



Universiteit
Leiden
The Netherlands

From intracluster medium dynamics to particle acceleration

Zhang, X.

Citation

Zhang, X. (2022, June 29). *From intracluster medium dynamics to particle acceleration*. Retrieved from <https://hdl.handle.net/1887/3421512>

Version: Publisher's Version

License: [Licence agreement concerning inclusion of doctoral thesis in the Institutional Repository of the University of Leiden](#)

Downloaded from: <https://hdl.handle.net/1887/3421512>

Note: To cite this publication please use the final published version (if applicable).

5

The *Planck* clusters in the LOFAR sky: Dynamic states and density fluctuations of the intracluster medium

X. Zhang, A. Simionescu, F. Gastaldello, D. Eckert, L. Camillini, R. Natale, H. Akamatsu, A. Botteon, R. Cassano, V. Cuciti, L. Bruno, T.W. Shimwell and J.S. Kaastra

(To be submitted)

Abstract

Context: The recent second data release of the LOFAR Two-metre Sky Survey (LoTSS-DR2) contains detections of 83 radio halos in *Planck* Sunyaev-Zeldovich (SZ) selected galaxy clusters, providing an excellent opportunity to statistically study the properties of radio halos.

Aims: We aim to investigate the relation between cluster dynamic state and radio halo power. Meanwhile, we attempt to search for connections between thermal and non-thermal characteristics of radio halos in LoTSS-DR2.

Methods: We analyzed *XMM-Newton* and *Chandra* archival X-ray data of all *Planck* SZ clusters in the footprint of LoTSS-DR2. We computed concentration parameters and centroid shifts that indicate the dynamic states of the clusters. Furthermore, we performed power spectral analysis of the X-ray surface brightness fluctuations to investigate large scale density perturbations and estimate the turbulent velocity dispersion.

Results: The concentration parameters measured by the two telescopes are in good agreement, while the centroid shift has a larger scatter. The telescope point spread function and limited count number can both contribute to the discrepancy of morphological parameters. Meanwhile, uncertainties in X-ray background evaluation also worsen the accuracy of the concentration parameter. The cluster relaxation state is marginally anti-correlated with the amplitude of surface brightness

and density fluctuations on large scales, while we do not find a correlation between the amplitude of density fluctuations and radio halo power or emissivity at 150 MHz. Nevertheless, the injected power for particle acceleration calculated from turbulent dissipation is correlated with the radio halo power, where the best-fit unity slope implies that the injected power from turbulence is proportional to the radiative loss that is observed at 150 MHz.

5.1 Introduction

Radio halos are extended radio sources widely observed at the centers of galaxy clusters. They are unpolarized, with size of \sim Mpc and having steep spectra with spectral index¹ smaller than -1 (see the review of van Weeren et al. 2019). The synchrotron nature of radio halos indicates relativistic cosmic rays (CRs) and magnetic fields permeating the intracluster medium (ICM). Among all proposed origins of CRs for radio halos, ICM turbulent acceleration is the most plausible in-situ mechanism (see the review of Brunetti & Jones 2014). Radio halos have been found to be associated with a number of cluster X-ray properties. Their radio power \mathcal{P}_ν is correlated with cluster X-ray luminosities L_X (Giovannini et al. 1999; Kempner & Sarazin 2001; Cassano et al. 2013; Kale et al. 2015). The presence of radio halos is statistically higher in dynamically disturbed clusters (Cassano et al. 2010). Moreover, the dynamic state of clusters can partially explain the scatter in the \mathcal{P}_ν - L_X diagram (Yuan et al. 2015).

To better understand the role that turbulence plays in accelerating CRs in galaxy clusters, one approach is to map turbulent velocity dispersions in the ICM and search for their correlations with radio properties. The direct way of mapping ICM turbulent velocity fields in galaxy clusters uses X-ray emission line broadening (Zhuravleva et al. 2012), which requires high spectral resolution and is beyond the capability of current X-ray imaging spectrometers. The alternative way is using power spectra to measure density fluctuations as a proxy of the turbulent velocity dispersion (e.g. Churazov et al. 2012; Gaspari et al. 2014; Zhuravleva et al. 2014a). The first attempt of connecting turbulent velocity dispersion and radio halo properties was made by Eckert et al. (2017, hereafter E17), who used the power spectral method to measure the velocity dispersion σ_v for 51 galaxy clusters and studied the turbulent Mach number distribution, concluding that \mathcal{P}_ν is strongly correlated with σ_v .

¹ $S_\nu \propto \nu^\alpha$

The ongoing Low Frequency Array (LOFAR) Two-meter Sky Survey (LoTSS) (Shimwell et al. 2017) is powerful for systematic detection of radio halos in the northern hemisphere. In the footprint of the second LoTSS Data Release (LoTSS-DR2) (Shimwell et al. 2022), which covers 27% of the northern sky, we found 83 *Planck*-Sunyaev-Zeldovich DR2 (PSZ2) clusters (Planck Collaboration et al. 2016) hosting radio halos (Botteon et al. 2022, hereafter Paper I). The LoTSS-DR2-PSZ2 sample provides an excellent opportunity to systematically study the properties of radio halos in a mass-selected cluster sample. This is the sixth paper of the series. In this work, we focus on the X-ray properties and their connections to the radio halo properties of the PSZ2 clusters in the LoTSS-DR2 footprint. The data analysis includes two major parts. In the first part, we will compute two morphological parameters that indicate cluster dynamic states and discuss the discrepancy of measurements from different X-ray telescopes. The morphological parameters will be used in Cassano et al. (in prep.) for studying the radio halo occurrences and Cuciti et al. (in prep.) for studying the radio halo scaling relations. In the second part, we will compute large scale surface brightness (SB) and ICM density fluctuations. Using the density fluctuations, we estimate the turbulent velocity dispersion and explore its connection with radio halo power.

In this paper, we adopt a Lambda cold dark matter cosmology model with cosmological parameters $\Omega_M = 0.3$, $\Omega_\Lambda = 0.7$ and $h_0 = 0.7$.

5.2 X-ray sample

The LoTSS-DR2 footprint covers 309 PSZ2 clusters. We use archival *XMM-Newton* European Photon Imaging Camera (EPIC) and *Chandra* Advanced CCD Imaging Spectrometer (ACIS) data for X-ray analysis. There are 115 and 110 PSZ2 clusters with *Chandra* and *XMM-Newton* observations, respectively. The data availability of individual PSZ2 clusters are listed in table 1 of Paper I, while image products are available on the project website². The locations of clusters with available data are plotted in Fig. 5.1 and the sample sizes for different analysis are summarized in Table 5.1.

²https://lofar-surveys.org/planck_dr2.html

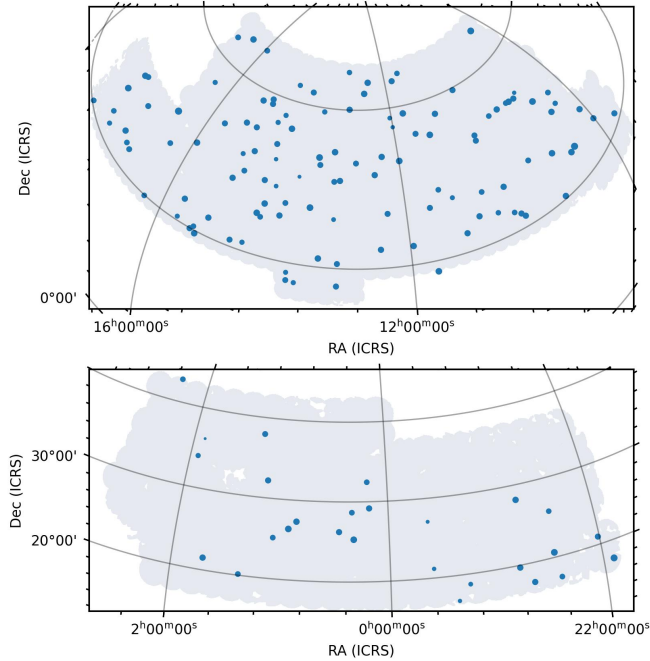


Figure 5.1: Footprint of the LoTSS-DR2 overlaid with locations of the PSZ2 clusters with available X-ray data. The marker size indicates the cluster mass.

Table 5.1: Summary of sample size in different steps.

Step	<i>Chandra</i>	<i>XMM-Newton</i>	Both	Total
A	115	110	72	153
B	105	98	63	140
C	107	109	66	150
D	–	64	–	64
E	–	36	–	36

A has archival data;

B has morphological parameter measurements;

C counting subclusters as individual clusters;

D meets criteria for power spectral analysis;

E has power spectra covering $k = (0.4 \times r_{500})^{-1}$.

5.2.1 Sample for morphological analysis

The summary of the X-ray sample used for morphology analysis is described in sect. 3.4 of Paper I. In short, we applied several criteria including field of view coverage, observation mode and image data quality to select the subsample for analysis. There are 140 clusters for which we derived morphological parameters. Among these clusters, 105 were observed by *Chandra*, and 98 by *XMM-Newton*. Some PSZ2 objects are composed of multiple separate subclusters in X-rays. Taking all extended X-ray sources into account, there are 107 and 109 subclusters with *Chandra* and *XMM-Newton* measurements, respectively. The total number of subclusters with morphological parameters is 150.

5.2.2 Sample for power spectral analysis

Power spectral analysis for SB fluctuations requires more counts than calculating morphological parameters. Therefore, we used an additional criterion of $> 10^4$ net X-ray counts in the annulus between 100 kpc and r_{2500} to select a subsample for SB power spectral analysis. Sixty-nine out of the total 109 *XMM-Newton* (sub)clusters meet the criterion. Among them, we excluded several objects that are in a complex merger state, which cannot be well modeled by a typical (double) β -model. They are PSZ2 G093.94-38.82 ES and EN, which are in a late pre-merger phase; PSZ2 G124.20-36.48 N and S (Abell 115), which is an offset major merger after first core passage. In addition, we excluded PSZ2 G160.83+81.66 for analysis due to its high redshift of 0.88. We also checked *Chandra* archival data. Since *Chandra* has only 1/3 of the effective area of *XMM-Newton*, we searched for clusters with total ACIS-I exposure > 80 ks and found that all clusters that meet this criterion have available *XMM-Newton* observations. Because we only investigate surface brightness fluctuations on large scales, where the *XMM-Newton* point spread function (PSF) size is not an issue, we did not include the *Chandra* data for analysis. Therefore, we have a sample size of 64 for analysis.

The cluster masses listed in Paper I are retrieved from Planck Collaboration et al. (2016), which are estimated from the Compton- y parameter of each PSZ2 object and are close to the total mass for systems with multiple subclusters that are not resolved by *Planck*. For systems showing multiple components in the X-ray images, We searched for mass ratios in the literature to accurately obtain r_{500} values for individual subclusters. If weak

lensing analyses are available, we prefer to use the weak lensing mass. PSZ2 G058.29+18.55 (Lyra complex) has a mass ratio of 2:1 between the E and W subclusters (Clavico et al. 2019); PSZ2 G107.10+65.32 (Abell 1758) has weak lensing mass of $M_{500,N} = 9.6 \times 10^{14} M_{\odot}$ and $M_{500,S} = 3.7 \times 10^{14} M_{\odot}$ for the N and S subclusters, respectively (Monteiro-Oliveira et al. 2017); PSZ2G093.94-38.82 (Abell 2572) has no literature of mass estimation and the PSZ centroid is located at the W subcluster, thus we use 2/3 of the total PSZ2 mass $1.5 \times 10^{14} M_{\odot}$ as the mass of the W subcluster.

5.3 Data reduction and spectral analysis

We used the *XMM-Newton* Science Analysis Software (SAS) v18.0.0 and Chandra Interactive Analysis of Observations (CIAO) v4.12 (Fruscione et al. 2006) for data reduction and analysis. The detailed reduction, image processing and point source detection methods are described in sect. 3.4 of Paper I. In this section, we describe our method of spectral analysis and *XMM-Newton* EPIC-pn non X-ray background (NXB) scaling. The pn filter wheel closed (FWC) version we used is 2019v1.

5.3.1 XMM-Newton EPIC spectral analysis

We used event selection criteria `#XMMEA_EM&&PATTERN<=12` and `FLAG==0&&PATTERN<=4` to extract MOS and pn spectra, respectively. Redistribution matrix files and auxiliary response files were generated by the tasks `rmfgen` and `arfgen`, respectively.

We used SPEX v3.06 (Kaastra et al. 1996; Kaastra et al. 2020a) for spectral analysis. Since most of our objects have a temperature $kT > 2$ keV based on the $M - kT$ scaling relations (Mantz et al. 2016), we used the atomic database SPEXACT v2.07 which includes less lines for fast calculation. We used the spectral model combination $cie1 \times red \times abs + cie2 \times abs + pow$, where the two *cies* are collisional ionization equilibrium models for the ICM and the foreground Galactic halo, *red* the redshift of the object, *abs* the Galactic absorption, *pow* the power law for the cosmic X-ray background (CXB). For *cie1*, the abundances of metal elements are coupled to Fe and we set the lower limit as 0.3 proto-solar (Lodders et al. 2009). The temperature for *cie2* is fixed to 0.2 keV (Snowden et al. 1998), the normalization of *abs* is set to the value from the database `nhtot`³ (Willingale

³<https://www.swift.ac.uk/analysis/nhtot/index.php>

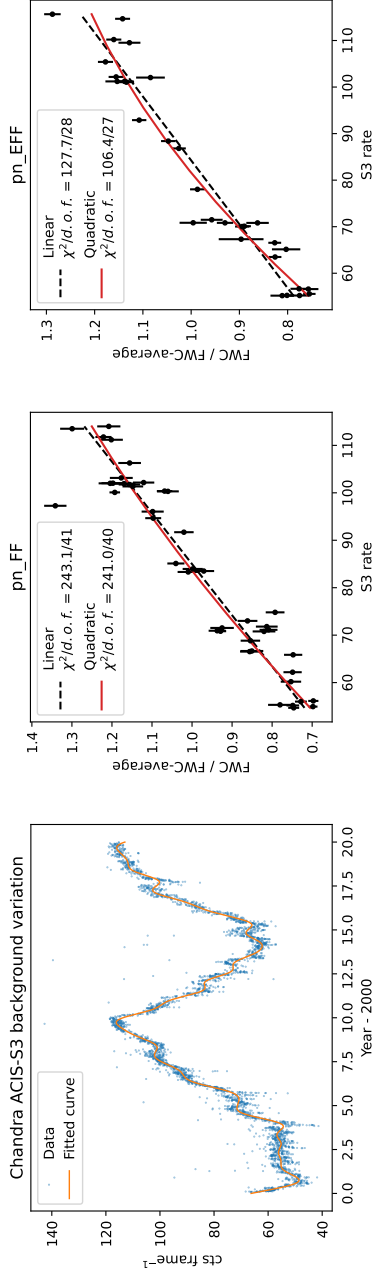


Figure 5.2: *Left:* Long term light curve of the Chandra ACIS-S3 particle background. *Middle and right:* EPIC-pn versus ACIS-S3 NXB levels for the FF and EFF observation modes, respectively. For both modes, a quadratic model (red) better fits the ratio than a linear model (black dashed).

et al. 2013). The photon index of *pow* is fixed to 1.41 (De Luca & Molendi 2004). We binned the spectra using the optimal binning algorithm (Kaas-stra & Bleeker 2016) and used the energy range 0.7–7.0 keV for spectral fitting. The Cash-statistic (Cash 1979) was adopted for calculating likelihood when optimizing parameters.

5.3.2 pn background scaling

XMM-Newton observations suffer from soft proton flares severely. Therefore, we need unexposed regions on the detectors to evaluate the level of the instrumental background. Different from the two EPIC-MOS detectors, there is no clean out of field of view (OoFoV) area on the four corners of the detector (e.g. Zhang et al. 2020; Marelli et al. 2021), i.e., the pn NXB level of each observation cannot be estimated using the OoFoV regions.

The particle backgrounds of both *XMM-Newton* and *Chandra* show long term variation that is anti-correlated with the solar activity (Gastaldello et al. 2022). We use *Chandra* ACIS-S3 long term monitoring data⁴ as a reference to predict the NXB level of the pn detector for any given epoch. We first fit the ACIS-S3 light curve using a Gaussian process regression method (Ambikasaran et al. 2015) with the *George* 0.4.0 package⁵. We adopted the product of an exponential squared kernel and a cosine kernel to represent the short term stochastic and long term periodic variation. The light curve and the fitted model are plotted in the left panel of Fig. 5.2.

We compared the pn FWC background 12–14 keV count rate with the predicted ACIS-S3 background count rate at each epoch of the calibration observations. We used a linear model and a quadratic model to fit the diagrams, respectively. χ^2 is used to evaluate the goodness of fit. We found that, for both the full-frame (FF) and extended-full-frame (EFF) observation mode, the diagrams are somewhat better fitted by quadratic models (see the middle and right panels of Fig. 5.2). We therefore applied the two quadratic models to science observations. For each observation epoch, we first predicted the ACIS-S3 NXB rate using the best-fit Gaussian process regression model, then we calculated the corresponding pn NXB rate either in FF or EFF modes based on the two quadratic models. We list the best-fit parameters for the two quadratic models in Table 5.2.

We evaluated the uncertainty of this method by calculating the stan-

⁴<https://space.mit.edu/~cgrant/cti/cti120.html>

⁵<https://github.com/dfm/george/tree/v0.4.0>

Table 5.2: Best-fit quadratic function parameters for scaling pn NXB.

Mode	a	b	c
FF	-0.000024	0.013	0.064
EFF	-0.000048	0.015	0.042

Note: The function is $y = ax^2 + bx + c$.

dard deviation of the residuals of the quadratic fitting. The standard deviations are 5.7% and 3.8% for the FF and EFF modes, respectively.

5.4 Morphological parameters

To investigate the connection between radio halos and cluster dynamic states in this series of papers, we adopt two X-ray morphological parameters. They are:

- concentration parameter (Santos et al. 2008),

$$c = \frac{F(r < r_{\text{core}})}{F(r < r_{\text{ap}})}, \quad (5.1)$$

where F is the X-ray flux, r_{core} is the aperture of the core region, r_{ap} is the outer aperture;

- centroid shift (Mohr et al. 1993; Poole et al. 2006),

$$w = \left[\frac{1}{N_{\text{ap}} - 1} \sum_i (\Delta_i - \bar{\Delta})^2 \right]^{1/2} \frac{1}{r_{\text{ap}}}, \quad (5.2)$$

where N_{ap} is the number of apertures, Δ_i the centroid for the i th aperture, $\bar{\Delta}$ the average centroid.

Following the convention of Cassano et al. (2010), we set $r_{\text{core}} = 100$ kpc and $r_{\text{ap}} = 500$ kpc. For the purpose of determining the centers of the analysis apertures, we smoothed both *XMM-Newton* and *Chandra* images and used the maximum intensity pixel after point source subtraction as the center of the analysis aperture. For parameter calculation, we input $\sigma = 30$ kpc Gaussian smoothed *Chandra* images but unsmoothed *XMM-Newton* images. The *Chandra* flux images were generated by subtracting the

blank-sky backgrounds that include CXB emission, while the background maps used for generating *XMM-Newton* flux images are NXB maps. Therefore, we subtract from the *XMM-Newton* images a universal constant as the CXB before calculating the morphological parameters. The universal value $S_{\text{CXB}} = 2.3 \times 10^{-6} \text{ cts s}^{-1} \text{ cm}^{-2} \text{ arcmin}^{-2}$ is the mean value of the cluster-free regions beyond r_{200} in the images of $z > 0.3$ clusters.

5.4.1 Individual measurements

In table 2 of Paper I, we presented single c and w measurements for all individual clusters. We note that for clusters with both usable *XMM-Newton* and *Chandra* data, the values are the mean values of the two measurements; the uncertainties are combinations of statistic and systematic uncertainties. We ask readers to refer to eqs. 3 and 4 of Paper I for the calculations. In this work, we present individual *XMM-Newton* and *Chandra* measurements of c and w in Table 5.3.

By comparing morphological parameters from two independent telescopes, we are able to evaluate the systematic uncertainties introduced during observations and data processing. We have 65 (sub)clusters that have morphological parameters measured by both *XMM-Newton* and *Chandra*. The *Chandra* versus *XMM-Newton* measurements of c and w are plotted in Fig. 5.3, where the insets in each panel illustrate the discrepancy of the measurements. In the next two subsections, we will explore the origins of the discrepancies.

5.4.2 Discrepancy in concentration parameter

In general, the c measurements from the two telescopes agree with each other well, with a mean deviation of 7% and a scatter of 11%. If we divide the sample into two different redshift ranges, the c from *Chandra* measurements are overall 15.3% and 5.3% higher than the *XMM-Newton* measurements, for the high redshift ($z > 0.3$) and low redshift ($z < 0.3$) populations, respectively.

The PSF of the telescopes is one of the major origins of the discrepancy in c , especially for distant cool core clusters, i.e., a large PSF smooths the core and leads to an underestimation of c . The result of the high redshift population agrees with this explanation. This discrepancy can be corrected if one recovers c from a surface brightness profile that takes instrumental PSF into account (e.g. Lovisari et al. 2017). However, for the low redshift

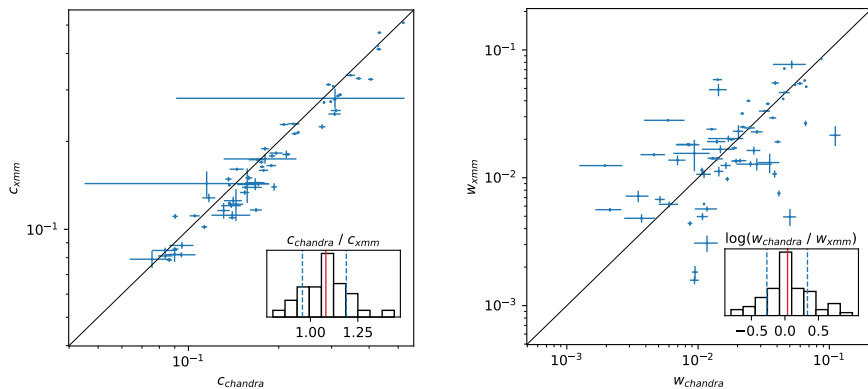


Figure 5.3: *Chandra* versus *XMM-Newton* measurements of c (left) and w (right), where black lines are diagonal. In each panel, the subplot is the histogram of the ratio between the measurements from the two telescopes. Red and blue dashed vertical lines indicate the mean and 1σ of the distributions, respectively. The large error bars of two *Chandra* c measurements are due to low count numbers.

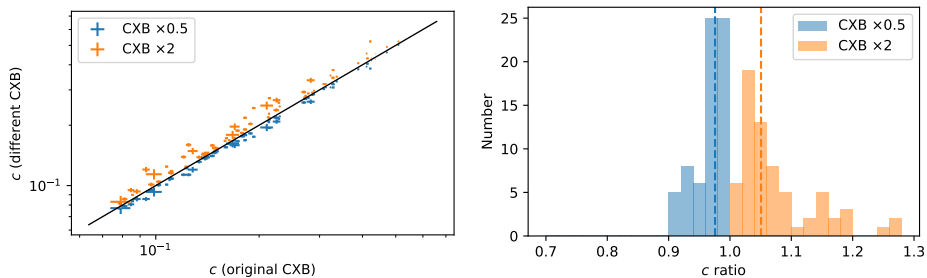


Figure 5.4: *Left:* Comparisons between c calculated using doubled (orange) and halved (blue) CXB levels and the original level for *XMM-Newton* clusters. The solid line is the diagonal. *Right:* Histograms of the discrepancy of the c values with doubled (orange) and halved (blue) CXB levels. The dashed lines denote median values of the two distributions.

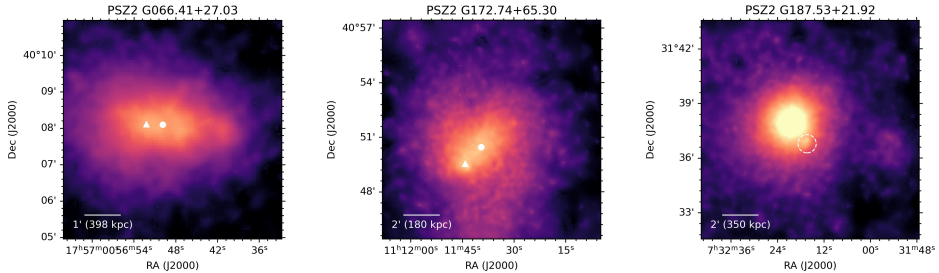


Figure 5.5: Examples of clusters with $w_{\text{Chandra}} \gg w_{\text{XMM}}$ (*left* and *middle*) and $w_{\text{Chandra}} \ll w_{\text{XMM}}$ (*right*). Triangle and point markers indicate the maximum intensity coordinates of the *Chandra* and *XMM-Newton* images, respectively. The dashed circle masks the residual of a point source near the bright core.

objects, the effect of the PSF should not be the case. In our analysis, we already smoothed the *Chandra* image with a 30 kpc kernel before the calculation, but not for the *XMM-Newton* image. This approach will make the smoothness of the *Chandra* images comparable to the *XMM-Newton* images at $z \sim 0.3$ and even higher for objects at lower redshifts, which means that PSF is not the only effect for the observed discrepancy. Therefore, we additionally check the systematic uncertainty due to CXB subtraction for low- z *XMM-Newton* clusters. We examined the discrepancy if increasing or decreasing the CXB level by a factor of two, respectively. The corresponding discrepancies are plotted in Fig. 5.4. A universal halved or doubled CXB levels can decrease or increase the measured c with median shifts of 2.5% and 5.1%. This analysis suggests that for our low- z *XMM-Newton* subsample, the CXB level could be globally higher than the universal value we use, which is obtained from the high- z subsample. This could be due to the large angular sizes of the low- z clusters, where more point sources are hidden behind the ICM emission and are not detected. This effect will be stronger on *XMM-Newton* observations due to its one order of magnitude larger PSF size than that of *Chandra*, and therefore is less sensitive to detect point sources in a cluster field.

Though *XMM-Newton* and *Chandra* have different instrumental properties, the measured c values are close enough for classifying cluster dynamic states in terms of the significance of the core. Our results extend the conclusion of Yuan & Han (2020) to a cross-instrument level, where they compared their *Chandra* c measurements with those in literature using dif-

ferent core-outer radii configurations (e.g. Cassano et al. 2013; Donahue et al. 2016; Andrade-Santos et al. 2017), and found that all the c measurements agree well.

5.4.3 Discrepancy in centroid shift

The centroid shift measurements show a larger discrepancy between the two telescopes. The distribution of $w_{\text{Chandra}}/w_{\text{XMM}}$ has a mean of 0.03 dex and a 1σ scatter of 0.34 dex. We did not find a redshift dependence of the ratio. Yuan & Han (2020) showed that the results of w have large discrepancy among different works, even if these are all with *Chandra* measurements.

We selected several objects with the largest difference to investigate the origin of the difference. We have five sources with discrepancies larger than $2\sigma_{\text{sys}}$. Among them, G187.53+21.92 and G192.18+56.12 have much larger w_{XMM} , while G172.74+65.30, G092.69+59.92 and G066.41+27.03 have much larger w_{Chandra} .

For those clusters with $w_{\text{Chandra}} \gg w_{\text{XMM}}$, G092.69+59.92 is faint in the shallow *Chandra* image, which could lead to a large uncertainty. For the remaining two objects, we checked the coordinates of the aperture centers in maps of the two instruments and found large distances between them (see the left and middle panel of Fig. 5.5). The two clusters do not host bright cool cores, which means that the uncertainty of the maximum intensity pixel is based on count number. In addition, the count numbers of the *XMM-Newton* images are much larger than the *Chandra* images, suggesting that the X-ray peaks of *Chandra* images have large uncertainty, leading to overestimations of the w . The overestimation of w due to low count numbers is similar to the findings of Nurgaliev et al. (2013), where they also analyzed *Chandra* data and used similar $\sigma = 40$ kpc Gaussian convolved images to determine the centroid. Despite the overestimate of w , we note that due to the flat morphology of the two clusters, even though the X-ray peaks determined by the two telescopes are different, measurements of c agree with each other within a 10% level.

For the two $w_{\text{Chandra}} \ll w_{\text{XMM}}$ objects, we found that the cluster PSZ2 G187.53+21.92 has a peaked morphology and there is a residual of a point source filling near the core in the *XMM-Newton* image (see the right panel of Fig. 5.5). Due to the non-negligible PSF of *XMM-Newton*, if a bright point source is near the cool core, the traditional point source removing

process⁶ cannot work perfectly due to the large gradient of the ICM emission. We also find a point source residual in G056.77+36.32, which is also a cluster with $w_{\text{Chandra}} \ll w_{\text{XMM}}$. However, we have no clear explanation for the discrepancy of G192.18+56.12.

5.4.4 Relaxation score

Recently, Ghirardini et al. (2021) proposed a novel method to combine the measurements of different morphological parameters into a new parameter, the relaxation score \mathcal{R} . The method calculates the joint cumulative probability function in a multi-dimensional parameter space. In our case, the joint cumulative distribution function in the space of c and w is

$$\mathcal{R}(c, w) = \int_{-\infty}^c \int_W^{\infty} f_{c,w}(c \leq C, w \geq W) dw dc, \quad (5.3)$$

where $f_{c,w}$ is the joint probability density function. Using this method, we are able to compare the degree of relaxation of clusters *within* our sample. We will use this parameter in the next section to explore the correlation between SB fluctuation and cluster dynamic state.

5.5 ICM density fluctuations on large scales

5.5.1 Calculation of 2D surface brightness fluctuations

The evaluation of the SB fluctuations, especially on large scales, is sensitive to the underlying SB model as illustrated in Zhuravleva et al. (2015) and Bonafede et al. (2018). For many clusters in our sample, the morphologies are clearly eccentric, which means a spherically symmetric β -model will lead to overestimation of the SB fluctuations. Therefore we used an elliptic β -model to fit the SB on large scales. For clusters with bright cool cores, we additionally used a second β -model to fit the core. For all clusters, we also added a constant model for the CXB during the fit. We fit the parameters directly in the 2D plane. The combination of the SB models can be written as

$$\begin{aligned} S_{\text{model}}(x, y) = & \text{Beta}(x, y, x_1, y_1, s_1, r_1, \beta_1) + \\ & E \text{Beta}(x, y, x_2, y_2, s_2, r_2, \beta_2, \theta_2, e_2) + \\ & C(s_3), \end{aligned} \quad (5.4)$$

⁶Such as https://cxc.cfa.harvard.edu/ciao/threads/diffuse_emission

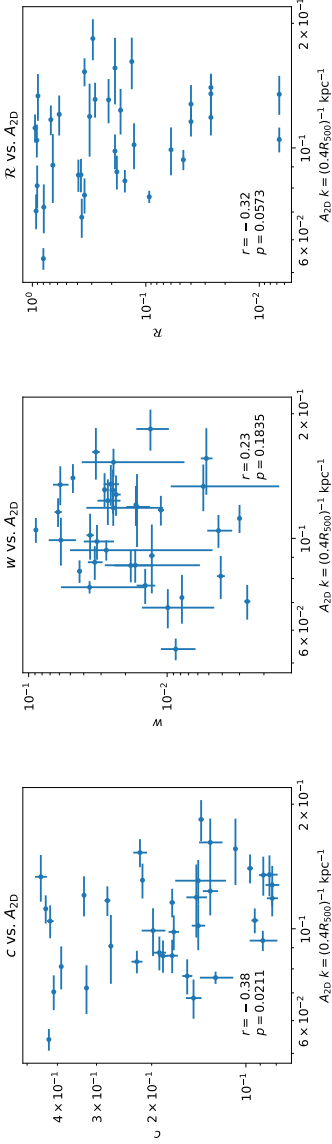


Figure 5.6: Morphological parameters c (left), w (middle) and relaxation score \mathcal{R} (right) versus A_{2D} . Pearson correlation coefficient and the corresponding p -value are labeled in each panel.

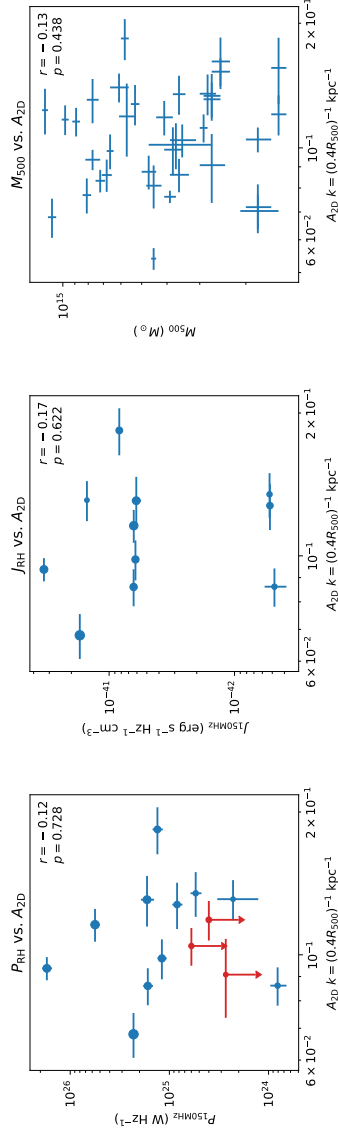


Figure 5.7: Radio halo power (left), radio halo emissivity (middle) and cluster mass (right) versus A_{2D} . Marker size in left and middle panels indicates cluster mass. Red points in the left panel indicate upper limits of radio halo power.

where $Beta$ is the 2D β -model describing the cores, $EBeta$ the 2D elliptical β -model describing the bulk ICM, C the constant model describing the sky background, x_i, y_i the center of the i th model in image coordinate, s_i the SB normalization, r_i the β -model core radius, β_i the β -model slope. The residual map is calculated as

$$\delta S(x, y) = \frac{[N_{\text{obs}}(x, y) - B(x, y)]/E(x, y) - C}{S_{\text{model}}(x, y) - C}, \quad (5.5)$$

where N_{obs} is the observed count image, E the vignetting corrected exposure map, B the NXB map. To measure the fluctuations contributed by Poisson noise, we simulate Poisson randomization of model count images and convert them to the flux regime. The simulated noise residual maps can be expressed as

$$\delta S_{\text{noise}}(x, y) = \frac{[N_{\text{rand}}(x, y) - B(x, y)]/E(x, y) - C}{S_{\text{model}}(x, y) - C}, \quad (5.6)$$

where

$$N_{\text{rand}} \sim \text{Pois}(\lambda = S_{\text{model}} \times E + B_{\text{smoothed}}), \quad (5.7)$$

is the Poisson randomization of the model count image, where B_{smoothed} is the smoothed NXB map. To minimize the uncertainty from the background, we choose $0.4r_{500}$ as the outer boundary for analysis, at which radius the flux from the ICM is approximately a factor of 2 higher than the sum of CXB and NXB.

We used a modified Δ -variance method (Arévalo et al. 2012) to calculate the 2D power spectra of the residual flux maps. This method cleanly compensates for data gaps and allows us to mask out regions of point sources and substructures of mergers. For each cluster, we obtained the power spectrum of SB fluctuation component $P_{2\text{D}}(k)$ ⁷ by subtracting the noise power spectrum from the power spectrum of the residual map, where we used a Monte-Carlo approach to simulate 100 noise maps using Eq. 5.6. At large wavenumbers, the total power spectrum is dominated by the noise component. Therefore, we set a cutoff at the wavenumber where the power of the fluctuation component is twice that of the noise component. The noise removed SB fluctuation power spectra were converted to 2D amplitude spectra using the equation

$$A_{2\text{D}}(k) = \sqrt{P_{2\text{D}}(k)2\pi k^2}. \quad (5.8)$$

⁷In this work, we adopt the definition of wave number $k \equiv 1/l$.

5.5.2 A_{2D} spectra and correlations with other parameters

E17 adopted a fixed scale of 660 kpc for calculating A_{2D} . Since our sample covers a wider range of mass, we adopt scales of $0.4 \times r_{500}$, which are close to 660 kpc for massive clusters. This scale also allows us to have at least two independent resolved components in the analysis aperture. After applying a wavenumber cut for each cluster, we have 36 objects whose A_{2D} spectra cover the wavenumber of $(0.4 \times r_{500})^{-1}$, where 11 objects have extended radio emission identified as radio halo. We note that the remaining 25 objects are not non radio halo clusters. Among them, 22 objects lack reasonable upper limits due to bad radio image quality, the presence of extended radio galaxies and residuals of source subtraction (Bruno et al. in prep.). Only three clusters have reasonable radio upper limits. The results of A_{2D} at $k = (0.4 \times r_{500})^{-1}$ are listed in the second column of Table 5.4.

We compared A_{2D} with morphological parameters (see Fig. 5.6). We calculated the Pearson correlation coefficients and corresponding p-values for $A_{2D}-c$, $A_{2D}-w$ and $A_{2D}-\mathcal{R}$ in logarithmic space. We found that A_{2D} is marginally anti-correlated with the concentration parameter c with a p-value of 0.021, whereas the p-value of $A_{2D}-w$ is 0.18, suggesting no correlation. As the combination of c and w , the relaxation score \mathcal{R} is also marginally anti-correlated with A_{2D} , where the p-value 0.057 is mostly driven by the weak anti-correlation between c and A_{2D} . We conclude that for our sample, the ICM dynamic state is marginally correlated with SB fluctuations at a scale of $0.4 \times r_{500}$, implying that more relaxed clusters tend to have smaller SB fluctuations on large scales.

We also explored the correlations between A_{2D} and radio halo power $\mathcal{P}_{150\text{MHz}}$, radio emissivity $J_{150\text{MHz}}$ and cluster mass M_{500} (see Fig. 5.7). The radio halo power and emissivity are obtained from Paper III. The upper limits of radio power are obtained from Paper V (Bruno et al. in prep.). The p-values of the three pairs are 0.73, 0.62 and 0.44, respectively, which means that at least in our sample, A_{2D} is independent of the radio halo power, emissivity and cluster mass.

5.5.3 Turbulent velocity dispersion

Theoretical work illustrated that weak ICM turbulent motions excite isobaric perturbations, in which condition the density fluctuation is proportional to the turbulent Mach number, which is $\delta\rho/\rho_0 \simeq \eta\mathcal{M}_{1D}$ (Gaspari et al. 2014). We estimated the turbulent velocity dispersion based on the

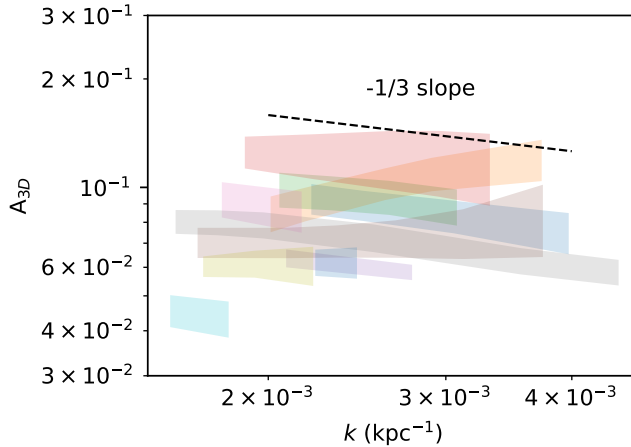


Figure 5.8: Recovered A_{3D} spectra for clusters with radio halo detection. The dashed line indicates the slope of Kolmogorov turbulent cascade.

following assumptions: 1) all surface brightness fluctuations are contributed by turbulent motions; 2) the triggered perturbations are isobaric; 3) the proportionality coefficient $\eta \simeq 1$ (Zhuravleva et al. 2014b) holds for both relaxed and merging clusters; 4) the ICM is isothermal in the radius of calculation, i.e. we use an average temperature to calculate the sound speed.

We used `pyproffit`⁸ (Eckert et al. 2020) to recover the 3D density fluctuations from 2D SB fluctuations. The process is the same as described in E17. In short, we constructed an ellipsoid for the 3D density distribution using the elliptical β -model in Eq. 5.4 and then computed the power spectrum of the normalized emissivity distribution along the line of sight to convert P_{2D} to P_{3D} (Churazov et al. 2012). The final A_{3D} spectrum was converted as

$$A_{3D}(k) = \sqrt{P_{3D}(k)4\pi k^3}. \quad (5.9)$$

The recovered A_{3D} spectra for the clusters hosting a radio halo are plotted in Fig. 5.8. Similar to A_{2D} , we took the value on the scale of $k = (0.4 \times r_{500})^{-1}$. The value of A_{3D} of each cluster is listed in the third column of Table 5.4. The A_{3D} values are linearly correlated with A_{2D} values, which means the relations of A_{2D} we obtained in Sect. 5.5.2 stand for A_{3D} as well.

⁸<https://github.com/domeckert/pyproffit>

For each cluster, the temperature is measured from a circular region with radius of $0.4 \times r_{500}$ centered at the X-ray centroid and with point sources and the center core component excluded. We excluded the MOS1 detector for spectral analysis because it has a chance to not cover the full region due to two missing chips. The measured temperatures are obtained following Sect. 5.3.1, and are listed in the fifth column of Table 5.4. We calculated the average sound speed within the region of analysis from the measured kT . The average ICM sound speed is $c_s = \sqrt{\gamma kT / \mu m_p} \simeq 507.3 \times \sqrt{kT / \text{keV}} \text{ km s}^{-1}$. The one dimensional Mach number \mathcal{M}_{1D} on the scale $1/k$ is identical to $A_{3D}(k)$ assuming $\eta = 1$. The three dimensional velocity dispersion is $\sigma_{v,3D} = \sqrt{3}\sigma_{v,1D} = \sqrt{3}\mathcal{M}_{1D}c_s$. The calculated $\sigma_{v,3D}$ values at $k = (0.4 \times r_{500})^{-1}$ are listed in the fourth column of Table 5.4.

By using the estimated 3D turbulent velocity dispersion, similar to E17, we explore its correlation to radio halo power (see the left panel of Fig. 5.9). The p-value of the Pearson correlation coefficient is 0.22, suggesting no correlation between radio power and turbulent velocity dispersion for our sample. Moreover, the velocity dispersions of the only three clusters with reliable radio upper limits are not lower than that of the population with radio halo detections. In the next section, we will further explore the connection between radio halo power and ICM properties from an angle of turbulent acceleration.

5.6 Relation between radio halo power and ICM thermodynamic properties

The radio halo power has been found to be correlated with the cluster mass (e.g. Cassano et al. 2006, 2007, 2013; Cuciti et al. 2021). With different sample selection functions and observation frequencies, the best-fit slopes in the $\mathcal{P}_\nu - M$ diagram range from 2.7 to 3.5 (Cuciti et al. 2021). Though we only have 11 clusters with both radio halo detection and velocity dispersion measurements, it is worthwhile to explore the relation between radio halo power and ICM properties using our measurements.

We inspected the relation between thermal and nonthermal phenomena in the scenario of turbulent acceleration assuming a quasi-steady state, which means the total amount of energy loss including synchrotron and the cosmic microwave background inverse Compton is balanced by the energy injection from acceleration. The turbulent dissipation rate per volume

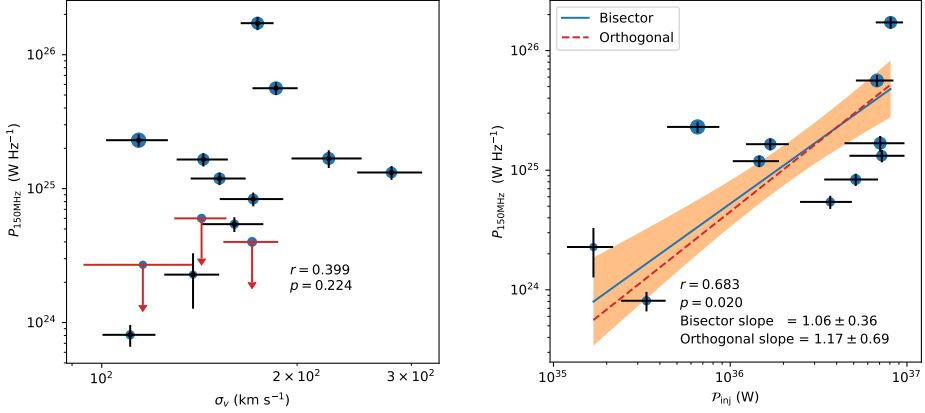


Figure 5.9: Radio halo power at 150 MHz versus turbulent velocity dispersion (*left*) and injection power from turbulent acceleration (*right*). Solid and dashed lines represent the best-fit results of BCES bisector and BCES Orthogonal, respectively. Orange band is the 1σ confidence band. Marker size indicates cluster mass.

is

$$\epsilon_{turb} = C_\epsilon \rho_{\text{gas}} \sigma_{v,k}^3 k, \quad (5.10)$$

where the coefficient C_ϵ is calculated from the Kolmogorov constant, although its value has been found not to be universal (e.g. Sreenivasan 1995). The dissipation rate itself is the total flux of kinetic energy loss, where kinetic energy can be converted into heat, magnetic energy and relativistic particles. We introduce a coefficient C_{TDD} to denote the proportion of dissipation to particle acceleration through transit-time damping resonance (e.g. Chandran 2000), which is the most important turbulent acceleration mechanism, and the value of C_{TDD} is up to a few percent (Brunetti & Lazarian 2007). In a Kolmogorov nature of the turbulence, $\sigma_{v,k} \propto k^{-1/3}$ and the term $\sigma_{v,k}^3 k$ is a constant when k is in the inertial range of the turbulent cascade. For the A_{3D} spectra of our radio halo sample (see Fig. 5.8), the slope is close to $-1/3$, therefore we assume the Kolmogorov nature and use $k = (0.4r_{500})^{-1}$ to estimate the dissipation rate. The total injection power of relativistic particles in the volume of the radio halo is

$$\mathcal{P}_{\text{inj}} = \int_{V_{\text{RH}}} C_{\text{TDD}} C_\epsilon \rho_{\text{gas}} \sigma_{v,k}^3 k \, dV. \quad (5.11)$$

Assuming the two coefficients and $\sigma_{v,k}^3 k$ are invariant throughout the vol-

ume of the radio halo, then Eq. 5.11 can be written as

$$\mathcal{P}_{\text{inj}} = C_{\text{TTD}} C_{\epsilon} \sigma_{v,k}^3 k M_{\text{gas}}(r_{\text{RH}}), \quad (5.12)$$

where r_{RH} is the radius of the radio halo. The injected power is then proportional to the gas mass inside the volume of radius r_{RH} .

Using Eq. 5.12, we estimated the power dissipated to particle acceleration for the 11 clusters. We first calculated the gas mass inside the volume of the radio halos in our sample. The 11 clusters do not show significant core components. Therefore, we extracted one dimensional SB profile for each cluster and fitted it using a simple projected density β -model (Cavaliere & Fusco-Femiano 1978), where the hydrogen number density n_{H} and projected surface brightness S_{X} are expressed as

$$n_{\text{H}}(r) = n_{\text{H},0} \left[1 + \left(\frac{r}{r_{\text{c}}} \right)^2 \right]^{-3\beta/2}, \quad (5.13)$$

$$S_{\text{x}}(r) = 2 \times \int_0^{\infty} n_{\text{H}}(\sqrt{l^2 + r^2})^2 \Lambda \, dl, \quad (5.14)$$

where Λ is the cooling function and is approximately a constant for $kT \gtrsim 2.5$ keV. The gas density can be converted from hydrogen number density as $\rho_{\text{gas}} \simeq 2.3 n_{\text{H}} \mu m_{\text{H}}$, where $\mu \simeq 0.6$ is the mean molecular weight. We integrated the gas mass using the best-fit density profile up to the radius of r_{RH} . Following Bonafede et al. (2017), we use 2.6 e -folding radii as the r_{RH} s. The e -folding radii are obtained from table 3 of Paper I. We set $C_{\epsilon} \simeq 5$ (Zhuravleva et al. 2014a) and arbitrarily set $C_{\text{TTD}} = 0.05$ (e.g. Brunetti & Lazarian 2007) to calculate \mathcal{P}_{inj} for our sample. The resulting $\mathcal{P}_{150\text{MHz}} - \mathcal{P}_{\text{inj}}$ diagram is plotted in the right panel of Fig. 5.9. Different from the result in the $\mathcal{P}_{\nu} - \sigma_{\nu}$ diagram, the corresponding p-value of the Pearson coefficient is improved to 0.020 in the $\mathcal{P}_{\nu} - \mathcal{P}_{\text{inj}}$ plane, which shows that the radio monochromatic power at 150 MHz is marginally correlated with the injected power from turbulent dissipation. We use the code BCES⁹, which uses the method taking bivariate correlated errors and intrinsic scatter into account (Akritas & Bershady 1996), to calculate the slope for our sample. The slope from the BCES bisector method is 1.06 ± 0.36 . Alternatively, the BCES orthogonal method returns a slope of 1.17 ± 0.60 . Both of the slopes from different methods agree with each other and are close to unity.

⁹<https://github.com/rsnemmen/BCES>

5.7 Discussion

The radio halo sample used in E17 is adopted from Cassano et al. (2013), where the mass range is $M_{500} > 6 \times 10^{14} M_{\odot}$ and the radio observation frequency is 1.4 GHz. The analysis of E17 has two main results. First, the A_{2D} distribution shows bimodality, where clusters with radio halos have higher SB fluctuations than clusters with only upper limits of radio halo. Second, the radio halo power at 1.4 GHz is correlated with the turbulent velocity dispersion with a best-fit slope of 3.3 ± 0.7 .

Our analysis cannot reproduce the first result directly, since among the 36 objects with A_{2D} measurements, only 11 have radio halo detections and 3 have reasonable image quality to estimate upper limits. We cannot put reasonable upper limits for the other 22 objects due to either bad radio image quality or the emission significantly suffering from calibration artifacts. Nevertheless, the anti-correlation we found in the c - A_{2D} plane (see Sect. 5.5.2) indirectly proves that radio halo clusters have higher A_{2D} than clusters without a radio halo. Statistical studies show that the occurrence of radio halos is significantly higher in clusters with low concentration parameter (e.g. Cassano et al. 2010; Cuciti et al. 2015). Clusters with higher SB fluctuations are more likely to host less dense cores and therefore have a higher probability to host radio halos.

Different from the second conclusion of E17, our analysis does not find a correlation between $\mathcal{P}_{150\text{MHz}}$ and σ_v . To investigate this disagreement, we revisit the $\mathcal{P}_{1.4\text{GHz}}-\sigma_v$ diagram of E17. We find that the Bullet Cluster and MACSJ0717 are included in that sample, which are two radio bright merging clusters that appear extremely disturbed in X-rays. Since an extremely disturbed morphology could overestimate the density fluctuation contributed by turbulent motions, we exclude the two clusters and compute the Pearson correlation coefficient again. For $\mathcal{P}_{1.4\text{GHz}}$ versus σ_v , the corresponding p-value increases from the original 2×10^{-6} to 0.05. However, it still suggests a marginal correlation. Therefore, besides the clusters with extremely disturbed morphology, the disagreement could be due to other factors. First, our sample size is half of the E17 sample, which means that it is more difficult to draw a statistically significant conclusion with a smaller sample. Second, the observation frequency of LoTSS is 150 MHz, which is an order of magnitude lower than the 1.4 GHz frequency used in E17. The energy of the CR population that is observed at 150 MHz is closer to that of the seed population, which means the density of that population

is less sensitive to acceleration efficiency. In this case, at low frequency, we will have more probability to observe ultra-steep spectrum radio halos (USSRHs) (e.g. Cuciti et al. 2021), which are below the detection limit in the GHz frequency bands. In other words, the radio halo sample in E17 only contains regular radio halos with relatively flat spectra, whereas the sample in our analysis could be the combination of USSRH and regular radio halos. The exact spectral nature of our sample needs to be further explored with high frequency follow-ups.

Though we did not find a correlation between the turbulent velocity dispersion and radio halo power for our sample, we successfully built up the scaling relation between injected turbulent power and the power emitted at 150 MHz (observer frame, k-correction applied) with a slope close to one. This slope suggests that the radio halo power, at least measured at 150 MHz, is determined not only by the turbulent velocity dispersion, but also by the ICM mass inside the radio halo volume. The two factors also reflect the underlying temperature - halo mass and baryonic mass - halo mass scaling relations. Since the high momentum CR population is more sensitive to the acceleration power, we speculate that the slope in the $\mathcal{P}_\nu - \mathcal{P}_{\text{inj}}$ will be steeper for samples at higher observation frequencies. This is the first time we search for the relation between radio halo power and turbulent dissipation rate with radio-X-ray synergy. The slope needs to be further investigated with a larger sample and a wider frequency range.

5.8 Conclusion

We analyzed archival *XMM-Newton* and *Chandra* X-ray data of PSZ2 clusters in the footprint of LoTSS-DR2. We computed two morphological parameters, i.e. concentration parameter and centroid shift. Meanwhile, we calculated the large scale surface brightness and density fluctuation amplitude and estimate the turbulent velocity dispersion.

The measurements of concentration parameter obtained with the two telescopes agree well with each other with a global discrepancy of $7 \pm 11\%$. On the contrary, the discrepancy of the centroid shifts from the two telescopes is large, with an rms of 0.34 dex. We found that, the concentration parameter measured by *Chandra* is globally higher than by *XMM-Newton*, and the difference is more significant for the high redshift population, which can be explained by the different PSF sizes of the two telescopes. Nevertheless the difference in c is only 15% at $z > 0.3$. For the

low redshift population, the underestimation of the CXB level could introduce the discrepancy in the concentration parameter. Both artifacts of point source removal and low count number can introduce systematics to the centroid shift measurement.

We found a marginal correlation between the large scale surface brightness amplitude and concentration parameter. However, we did not find correlations between surface brightness fluctuations and cluster mass, radio halo power or radio halo emissivity. Using the turbulent velocity dispersion estimated from density fluctuations, we calculated the injected flux of turbulent acceleration. The injected flux is well correlated with radio power at 150 MHz with a slope consistent with unity within the uncertainties, suggesting that the turbulent acceleration scenario can well connect the observed cluster thermodynamic properties to the nonthermal properties.

Acknowledgements

This work is based on observations obtained with *XMM-Newton*, an ESA science mission with instruments and contributions directly funded by ESA Member States and NASA. This research has made use of data obtained from the *Chandra* Data Archive and the *Chandra* Source Catalog, and software provided by the *Chandra* X-ray Center (CXC) in the application packages CIAO and Sherpa. This research made use of Astropy¹⁰, a community-developed core Python package for Astronomy (Astropy Collaboration et al. 2013, 2018).

¹⁰<http://www.astropy.org>

Table 5.3: Morphological parameters c and w measured using both XMM-Newton and Chandra images.

Name	Subcluster	c^{Chandra}	w^{Chandra}	c^{XMM}	w^{XMM}
PSZ2 G023.17+86.71		0.131 ± 0.006	0.0203 ± 0.0018	0.116 ± 0.007	0.0231 ± 0.0027
PSZ2 G031.93+78.71		—	—	0.2138 ± 0.0015	0.02826 ± 0.00024
PSZ2 G033.81+77.18		0.4270 ± 0.0014	0.01110 ± 0.00016	0.4242 ± 0.0007	0.00624 ± 0.00006
PSZ2 G040.58+77.12		0.224 ± 0.010	0.0060 ± 0.0010	0.2297 ± 0.0013	0.00620 ± 0.00033
PSZ2 G045.87+57.70		—	—	0.254 ± 0.005	0.0218 ± 0.0007
PSZ2 G046.88+56.48		0.0863 ± 0.0019	0.0219 ± 0.0012	0.0785 ± 0.0011	0.0250 ± 0.0005
PSZ2 G048.10+57.16		0.0905 ± 0.0021	0.0667 ± 0.0009	0.0856 ± 0.0008	0.0516 ± 0.0004
PSZ2 G048.75+53.18		0.340 ± 0.008	0.0065 ± 0.0012	—	—
PSZ2 G049.18+65.05		0.287 ± 0.017	0.0080 ± 0.0031	—	—
PSZ2 G049.32+44.37		0.180 ± 0.005	0.0111 ± 0.0014	0.1887 ± 0.0029	0.0106 ± 0.0007
PSZ2 G050.46+67.54		0.361 ± 0.005	0.0019 ± 0.0005	—	—
PSZ2 G053.53+59.52		0.1370 ± 0.0013	0.0167 ± 0.0005	0.1417 ± 0.0014	0.0098 ± 0.0004
PSZ2 G054.99+53.41		0.154 ± 0.005	0.0195 ± 0.0016	0.1337 ± 0.0024	0.0135 ± 0.0006
PSZ2 G055.59+31.85		0.315 ± 0.004	0.0095 ± 0.0005	0.2858 ± 0.0019	0.00183 ± 0.00021
PSZ2 G056.77+36.32		0.293 ± 0.006	0.0021 ± 0.0005	0.3129 ± 0.0014	0.00563 ± 0.00018
PSZ2 G057.61+34.93		0.105 ± 0.004	0.0139 ± 0.0016	0.1112 ± 0.0013	0.0141 ± 0.0005
PSZ2 G057.78+52.32	E	—	—	0.2256 ± 0.0018	0.0061 ± 0.0005
PSZ2 G057.78+52.32	W	—	—	0.225 ± 0.006	0.0161 ± 0.0014
PSZ2 G057.92+27.64		0.433 ± 0.006	0.0094 ± 0.0007	0.4712 ± 0.0022	0.00158 ± 0.00011
PSZ2 G058.29+18.55	E	0.140 ± 0.004	0.0141 ± 0.0011	0.1096 ± 0.0006	0.05856 ± 0.00022
PSZ2 G058.29+18.55	W	—	—	0.4215 ± 0.0033	0.0134 ± 0.0005
PSZ2 G059.47+33.06		0.405 ± 0.008	0.0130 ± 0.0012	0.3261 ± 0.0028	0.01423 ± 0.00030
PSZ2 G060.55+27.00		0.431 ± 0.008	0.0037 ± 0.0010	0.413 ± 0.004	0.0048 ± 0.0004
PSZ2 G062.94+43.69		—	—	0.43614 ± 0.00034	0.00300 ± 0.000019
PSZ2 G065.28+44.53		0.211 ± 0.007	0.0344 ± 0.0018	—	—
PSZ2 G066.41+27.03		0.095 ± 0.011	0.050 ± 0.006	0.0818 ± 0.0016	0.0049 ± 0.0008

Table 5.3: continued.

Name	Subcluster	C_{Chandra}	w_{Chandra}	C_{XMM}	w_{XMM}
PSZ2 G066.68+68.44		0.347 ± 0.012	0.0117 ± 0.0023	0.3366 ± 0.0021	0.00570 ± 0.00026
PSZ2 G067.17+67.46		0.2320 ± 0.0029	0.0445 ± 0.0006	0.2146 ± 0.0014	0.04139 ± 0.00024
PSZ2 G067.52+34.75		—	—	0.3888 ± 0.0024	0.00410 ± 0.00027
PSZ2 G068.36+81.81		—	—	0.1373 ± 0.0031	0.0269 ± 0.0008
PSZ2 G070.89+49.26		—	—	0.136 ± 0.004	0.0206 ± 0.0012
PSZ2 G071.21+28.86		—	—	0.064 ± 0.004	0.0129 ± 0.0021
PSZ2 G071.39+59.54		0.167 ± 0.009	0.0139 ± 0.0022	0.1392 ± 0.0031	0.0192 ± 0.0007
PSZ2 G071.63+29.78		0.084 ± 0.005	0.0383 ± 0.0017	0.0811 ± 0.0016	0.0107 ± 0.0007
PSZ2 G072.62+41.46		0.1370 ± 0.0018	0.0217 ± 0.0007	0.1228 ± 0.0016	0.0318 ± 0.0005
PSZ2 G073.31+67.52		0.167 ± 0.012	0.015 ± 0.004	0.144 ± 0.005	0.0167 ± 0.0012
PSZ2 G073.97+27.82		0.2830 ± 0.0014	0.01070 ± 0.00027	0.2718 ± 0.0028	0.0114 ± 0.0006
PSZ2 G074.37+71.11		0.143 ± 0.020	0.028 ± 0.006	—	—
PSZ2 G076.55+60.29		0.238 ± 0.017	0.029 ± 0.004	—	—
PSZ2 G077.90+26.63		0.226 ± 0.005	0.0189 ± 0.0009	0.2125 ± 0.0018	0.01715 ± 0.00026
PSZ2 G080.16+57.65		0.139 ± 0.011	0.0322 ± 0.0031	0.1205 ± 0.0021	0.0332 ± 0.0008
PSZ2 G080.41+33.24		0.2150 ± 0.0020	0.0454 ± 0.0005	0.1806 ± 0.0009	0.07153 ± 0.00019
PSZ2 G080.64+64.31		0.453 ± 0.012	0.0062 ± 0.0015	—	—
PSZ2 G081.02+50.57		—	—	0.149 ± 0.005	0.0377 ± 0.0014
PSZ2 G081.72+70.15		0.121 ± 0.018	0.018 ± 0.005	—	—
PSZ2 G083.29+31.03		0.189 ± 0.007	0.0404 ± 0.0022	0.1653 ± 0.0020	0.0191 ± 0.0004
PSZ2 G083.86+85.09		0.196 ± 0.010	0.0371 ± 0.0023	0.1824 ± 0.0022	0.0294 ± 0.0005
PSZ2 G084.10+58.72		0.18 ± 0.05	0.028 ± 0.008	0.174 ± 0.007	0.0128 ± 0.0014
PSZ2 G084.13+35.41		—	—	0.095 ± 0.006	0.0379 ± 0.0021
PSZ2 G084.69+42.28		—	—	0.270 ± 0.004	0.0129 ± 0.0006
PSZ2 G086.54+26.67		0.304 ± 0.006	0.0054 ± 0.0009	—	—
PSZ2 G086.93+53.18		0.140 ± 0.021	0.017 ± 0.005	0.112 ± 0.004	0.0203 ± 0.0011

Table 5.3: continued.

Name	Subcluster	c_{Chandra}	w_{Chandra}	c_{XMM}	w_{XMM}
PSZ2 G087.39+50.92		—	—	0.213 ± 0.012	0.0234 ± 0.0021
PSZ2 G088.98+55.07		0.31 ± 0.22	0.052 ± 0.015	0.281 ± 0.022	0.077 ± 0.006
PSZ2 G089.52+62.34		0.113 ± 0.009	0.0320 ± 0.0023	—	—
PSZ2 G091.79-27.00		—	—	0.073 ± 0.006	0.0454 ± 0.0025
PSZ2 G092.69+59.92		0.12 ± 0.07	0.111 ± 0.011	0.143 ± 0.014	0.022 ± 0.004
PSZ2 G092.71+73.46		0.159 ± 0.004	0.0163 ± 0.0015	0.1500 ± 0.0027	0.0125 ± 0.0008
PSZ2 G093.94-38.82	EN	—	—	0.2143 ± 0.0024	0.0407 ± 0.0006
PSZ2 G093.94-38.82	ES	—	—	0.1930 ± 0.0023	0.0318 ± 0.0006
PSZ2 G093.94-38.82	W	—	—	0.3285 ± 0.0031	0.0168 ± 0.0005
PSZ2 G094.44+36.13		0.310 ± 0.012	0.0085 ± 0.0017	0.2550 ± 0.0032	0.0181 ± 0.0005
PSZ2 G094.56+51.03		—	—	0.102 ± 0.004	0.0569 ± 0.0017
PSZ2 G094.61-41.24		—	—	0.3228 ± 0.0013	0.00782 ± 0.00022
PSZ2 G095.22+67.41		—	—	0.1246 ± 0.0023	0.0206 ± 0.0009
PSZ2 G096.83+52.49		0.209 ± 0.004	0.0087 ± 0.0009	—	—
PSZ2 G097.52+51.70		—	—	0.217 ± 0.008	0.0192 ± 0.0011
PSZ2 G097.72+38.12		0.1760 ± 0.0031	0.0242 ± 0.0008	0.1637 ± 0.0014	0.03998 ± 0.00032
PSZ2 G099.48+55.60		0.084 ± 0.008	0.0281 ± 0.0029	0.0847 ± 0.0019	0.0229 ± 0.0008
PSZ2 G099.86+58.45		0.141 ± 0.010	0.0266 ± 0.0032	0.125 ± 0.004	0.0163 ± 0.0012
PSZ2 G100.14+41.67		0.2500 ± 0.0030	0.0567 ± 0.0006	—	—
PSZ2 G100.45-38.42		—	—	0.4113 ± 0.0015	0.00264 ± 0.00014
PSZ2 G103.40-32.99		—	—	0.1076 ± 0.0012	0.0052 ± 0.0005
PSZ2 G105.55+77.21		—	—	0.1820 ± 0.0023	0.0252 ± 0.0006
PSZ2 G106.41+50.82		0.369 ± 0.008	0.0180 ± 0.0010	0.328 ± 0.004	0.0199 ± 0.0005
PSZ2 G106.61+66.71		0.140 ± 0.032	0.051 ± 0.008	—	—
PSZ2 G107.10+65.32	N	0.1130 ± 0.0026	0.0869 ± 0.0010	0.1019 ± 0.0017	0.0853 ± 0.0007
PSZ2 G107.10+65.32	S	0.1360 ± 0.0033	0.0340 ± 0.0012	0.1485 ± 0.0027	0.0379 ± 0.0007

Table 5.3: continued.

Name	Subcluster	c_{Chandra}	w_{Chandra}	c_{XMM}	w_{XMM}
PSZ2 G109.97+52.84		0.334 ± 0.005	0.0082 ± 0.0009	—	—
PSZ2 G111.75+70.37		0.095 ± 0.009	0.0596 ± 0.0030	0.0881 ± 0.0023	0.0547 ± 0.0010
PSZ2 G112.35-32.86		—	—	0.263 ± 0.010	0.0135 ± 0.0014
PSZ2 G112.48+56.99		0.174 ± 0.005	0.0046 ± 0.0010	—	—
PSZ2 G113.29-29.69		0.178 ± 0.006	0.0084 ± 0.0015	0.1592 ± 0.0015	0.0182 ± 0.0004
PSZ2 G113.91-37.01		0.171 ± 0.015	0.046 ± 0.004	0.1431 ± 0.0026	0.0464 ± 0.0007
PSZ2 G114.31+64.89		0.193 ± 0.004	0.0144 ± 0.0012	0.140 ± 0.004	0.0112 ± 0.0010
PSZ2 G114.79-33.71		0.145 ± 0.008	0.0117 ± 0.0024	0.1607 ± 0.0018	0.0031 ± 0.0004
PSZ2 G114.99+70.36		0.146 ± 0.006	0.0172 ± 0.0018	—	—
PSZ2 G116.32-36.33	N	0.157 ± 0.011	0.0094 ± 0.0029	0.142 ± 0.019	0.016 ± 0.004
PSZ2 G116.32-36.33	S	—	—	0.297 ± 0.013	0.0091 ± 0.0015
PSZ2 G116.50-44.47		—	—	0.130 ± 0.007	0.0560 ± 0.0024
PSZ2 G121.03+57.02		0.098 ± 0.008	0.110 ± 0.004	—	—
PSZ2 G121.13+49.64		—	—	0.099 ± 0.005	0.0328 ± 0.0019
PSZ2 G123.00-35.52		—	—	0.156 ± 0.005	0.0239 ± 0.0011
PSZ2 G123.66+67.25		0.250 ± 0.030	0.016 ± 0.005	—	—
PSZ2 G124.20-36.48	N	0.3040 ± 0.0029	0.0549 ± 0.0005	0.3086 ± 0.0025	0.05331 ± 0.00035
PSZ2 G124.20-36.48	S	0.0903 ± 0.0018	0.0251 ± 0.0007	0.1107 ± 0.0021	0.0128 ± 0.0006
PSZ2 G125.71+53.86		0.212 ± 0.006	0.0070 ± 0.0010	0.180 ± 0.005	0.0137 ± 0.0012
PSZ2 G126.61-37.63		—	—	0.170 ± 0.006	0.0088 ± 0.0011
PSZ2 G127.50-30.52		—	—	0.116 ± 0.007	0.0139 ± 0.0020
PSZ2 G132.54-42.16		—	—	0.211 ± 0.009	0.0026 ± 0.0016
PSZ2 G133.59+50.68		—	—	0.093 ± 0.005	0.0194 ± 0.0022
PSZ2 G133.60+69.04		0.087 ± 0.009	0.0380 ± 0.0035	—	—
PSZ2 G134.70+48.91		0.279 ± 0.007	0.0035 ± 0.0007	0.224 ± 0.004	0.0072 ± 0.0007
PSZ2 G135.17+65.43		0.105 ± 0.019	0.047 ± 0.008	—	—

Table 5.3: continued.

Name	Subcluster	c_{Chandra}	w_{Chandra}	c_{XMM}	w_{XMM}
PSZ2 G135.19+57.88		0.166 ± 0.009	0.0133 ± 0.0026	—	—
PSZ2 G136.92+59.46		—	—	0.0937 ± 0.0023	0.0887 ± 0.0012
PSZ2 G137.74-27.08		—	—	0.1462 ± 0.0024	0.0431 ± 0.0007
PSZ2 G138.32-39.82		0.198 ± 0.007	0.0132 ± 0.0013	—	—
PSZ2 G139.18+56.37		0.090 ± 0.004	0.0388 ± 0.0025	0.082 ± 0.005	0.0552 ± 0.0021
PSZ2 G143.26+65.24		0.168 ± 0.008	0.0247 ± 0.0024	0.1165 ± 0.0020	0.0245 ± 0.0006
PSZ2 G145.65+59.30		—	—	0.144 ± 0.007	0.0120 ± 0.0015
PSZ2 G148.36+75.23		0.206 ± 0.009	0.0527 ± 0.0024	—	—
PSZ2 G149.22+54.18		0.1360 ± 0.0034	0.0037 ± 0.0008	—	—
PSZ2 G149.75+34.68		0.1750 ± 0.0029	0.0649 ± 0.0010	0.1696 ± 0.0012	0.05768 ± 0.00028
PSZ2 G150.56+58.32		0.144 ± 0.008	0.0143 ± 0.0022	0.122 ± 0.015	0.049 ± 0.005
PSZ2 G151.19+48.27		0.076 ± 0.012	0.035 ± 0.006	0.079 ± 0.005	0.0131 ± 0.0023
PSZ2 G160.83+81.66		0.307 ± 0.014	0.0209 ± 0.0024	0.248 ± 0.004	0.0136 ± 0.0004
PSZ2 G163.69+53.52		0.198 ± 0.006	0.0083 ± 0.0014	—	—
PSZ2 G163.87+48.54		0.4610 ± 0.0035	0.00161 ± 0.00034	—	—
PSZ2 G164.65+46.37		0.246 ± 0.010	0.0605 ± 0.0021	—	—
PSZ2 G165.06+54.13		0.188 ± 0.005	0.0177 ± 0.0015	—	—
PSZ2 G165.46+66.15		0.070 ± 0.005	0.0331 ± 0.0031	—	—
PSZ2 G165.95+41.01		—	—	0.658 ± 0.028	0.042 ± 0.006
PSZ2 G166.09+43.38		0.190 ± 0.005	0.0127 ± 0.0011	0.1784 ± 0.0025	0.0240 ± 0.0005
PSZ2 G166.62+42.13		0.069 ± 0.006	0.0348 ± 0.0030	—	—
PSZ2 G168.33+69.73		0.264 ± 0.030	0.019 ± 0.004	—	—
PSZ2 G170.98+39.45		0.114 ± 0.016	0.027 ± 0.007	—	—
PSZ2 G172.63+35.15		0.184 ± 0.009	0.0201 ± 0.0021	—	—
PSZ2 G172.74+65.30		0.208 ± 0.006	0.0413 ± 0.0012	0.2284 ± 0.0019	0.0075 ± 0.0004
PSZ2 G175.60+35.47		0.266 ± 0.011	0.0105 ± 0.0020	—	—

Table 5.3: continued.

Name	Subcluster	C_{Chandra}	w_{Chandra}	C_{XMM}	w_{XMM}
PSZ2 G176.27+37.54		0.243 ± 0.017	0.019 ± 0.004	—	—
PSZ2 G179.09+60.12		0.520 ± 0.004	0.0087 ± 0.0004	0.5093 ± 0.0021	0.00439 ± 0.00018
PSZ2 G180.60+76.65		0.289 ± 0.006	0.0024 ± 0.0005	—	—
PSZ2 G180.88+31.04		—	—	0.101 ± 0.011	0.018 ± 0.004
PSZ2 G181.06+48.47		0.141 ± 0.011	0.0695 ± 0.0030	—	—
PSZ2 G182.59+55.83		0.2980 ± 0.0030	0.0051 ± 0.0004	0.2735 ± 0.0025	0.0068 ± 0.0004
PSZ2 G183.90+42.99		—	—	0.156 ± 0.005	0.0182 ± 0.0011
PSZ2 G184.68+28.91		0.307 ± 0.005	0.0108 ± 0.0010	0.2783 ± 0.0022	0.00497 ± 0.00032
PSZ2 G186.37+37.26		0.155 ± 0.004	0.0046 ± 0.0010	0.1391 ± 0.0016	0.0152 ± 0.0004
PSZ2 G186.99+38.65		0.199 ± 0.008	0.0385 ± 0.0021	—	—
PSZ2 G187.53+21.92		0.320 ± 0.005	0.0019 ± 0.0007	0.2890 ± 0.0018	0.01245 ± 0.00023
PSZ2 G189.31+59.24		0.245 ± 0.004	0.0476 ± 0.0008	—	—
PSZ2 G190.61+66.46		0.105 ± 0.016	0.029 ± 0.006	—	—
PSZ2 G192.18+56.12		0.170 ± 0.011	0.0059 ± 0.0020	0.1731 ± 0.0026	0.0282 ± 0.0006
PSZ2 G193.63+54.85		—	—	0.167 ± 0.007	0.0562 ± 0.0019
PSZ2 G194.98+54.12		0.184 ± 0.014	0.0607 ± 0.0035	—	—
PSZ2 G195.60+44.06	E1	—	—	0.094 ± 0.006	0.0194 ± 0.0024
PSZ2 G195.60+44.06	E2	0.117 ± 0.006	0.0659 ± 0.0019	0.128 ± 0.004	0.0267 ± 0.0013
PSZ2 G195.60+44.06	W1	—	—	0.283 ± 0.008	0.0086 ± 0.0010
PSZ2 G195.60+44.06	W2	—	—	0.0970 ± 0.0021	0.0479 ± 0.0007
PSZ2 G205.90+73.76		0.212 ± 0.018	0.0135 ± 0.0032	—	—

Table 5.4: Power spectral analysis results and temperature measurements of the sample.

Name	A_{2D}	A_{3D}	$\sigma_{v,3D}$ km s ⁻¹	kT keV
PSZ2G031.93+78.71	0.131 ± 0.013	0.089 ± 0.009	138 ± 13	3.27 ± 0.04
PSZ2G033.81+77.18	0.0540 ± 0.0033	0.0375 ± 0.0023	75 ± 5	5.392 ± 0.031
PSZ2G040.58+77.12	—	—	—	4.64 ± 0.09
PSZ2G046.88+56.48	0.128 ± 0.014	0.086 ± 0.010	171 ± 19	5.28 ± 0.10
PSZ2G048.10+57.16	0.135 ± 0.015	0.097 ± 0.010	160 ± 17	3.68 ± 0.04
PSZ2G049.32+44.37	—	—	—	4.87 ± 0.14
PSZ2G053.53+59.52	0.184 ± 0.021	0.125 ± 0.014	280 ± 32	6.76 ± 0.18
PSZ2G054.99+53.41	0.119 ± 0.024	0.085 ± 0.017	210 ± 40	7.84 ± 0.27
PSZ2G055.59+31.85	—	—	—	7.28 ± 0.13
PSZ2G056.77+36.32	—	—	—	4.86 ± 0.05
PSZ2G057.61+34.93	—	—	—	4.57 ± 0.09
PSZ2G057.78+52.32E	—	—	—	2.98 ± 0.08
PSZ2G057.92+27.64	0.134 ± 0.017	0.090 ± 0.012	145 ± 19	3.51 ± 0.05
PSZ2G058.29+18.55E	0.0762 ± 0.0026	0.0512 ± 0.0017	91.2 ± 3.1	4.28 ± 0.04
PSZ2G058.29+18.55W	—	—	—	2.63 ± 0.18
PSZ2G059.47+33.06	—	—	—	6.79 ± 0.16
PSZ2G060.55+27.00	0.104 ± 0.010	0.071 ± 0.006	143 ± 13	5.47 ± 0.15
PSZ2G062.94+43.69	0.112 ± 0.009	0.073 ± 0.006	107 ± 8	2.868 ± 0.009
PSZ2G066.41+27.03	0.094 ± 0.005	0.0629 ± 0.0035	174 ± 10	10.29 ± 0.31
PSZ2G066.68+68.44	—	—	—	5.05 ± 0.07
PSZ2G067.17+67.46	0.083 ± 0.005	0.059 ± 0.004	152 ± 10	9.03 ± 0.16

Table 5.4: continued.

Name	A_{2D}	A_{3D}	$\sigma_{v,3D}$ km s ⁻¹	kT keV
PSZ2G067.52+34.75	0.081 ± 0.010	0.056 ± 0.007	107 ± 13	4.92 ± 0.12
PSZ2G068.36+81.81	—	—	—	6.77 ± 0.32
PSZ2G071.39+59.54	—	—	—	6.37 ± 0.22
PSZ2G071.63+29.78	0.119 ± 0.011	0.084 ± 0.008	170 ± 17	5.52 ± 0.17
PSZ2G072.62+41.46	0.123 ± 0.016	0.087 ± 0.011	233 ± 30	9.67 ± 0.25
PSZ2G073.97-27.82	0.117 ± 0.010	0.078 ± 0.006	200 ± 17	8.90 ± 0.24
PSZ2G077.90-26.63	—	—	—	4.96 ± 0.07
PSZ2G080.16+57.65	0.162 ± 0.023	0.109 ± 0.016	197 ± 28	4.35 ± 0.13
PSZ2G080.41-33.24	0.099 ± 0.013	0.065 ± 0.009	143 ± 19	6.44 ± 0.08
PSZ2G083.29-31.03	—	—	—	8.74 ± 0.29
PSZ2G083.86+85.09	0.088 ± 0.008	0.060 ± 0.006	123 ± 12	5.59 ± 0.13
PSZ2G084.69+42.28	0.091 ± 0.017	0.064 ± 0.012	116 ± 22	4.45 ± 0.15
PSZ2G092.71+73.46	0.077 ± 0.007	0.054 ± 0.005	124 ± 12	7.12 ± 0.24
PSZ2G093.94-38.82W	0.121 ± 0.013	0.081 ± 0.009	115 ± 13	2.71 ± 0.09
PSZ2G094.44+36.13	—	—	—	3.77 ± 0.14
PSZ2G094.61-41.24	0.072 ± 0.010	0.049 ± 0.007	72 ± 10	2.882 ± 0.021
PSZ2G095.22+67.41	—	—	—	2.86 ± 0.15
PSZ2G097.72+38.12	0.098 ± 0.009	0.070 ± 0.007	152 ± 15	6.26 ± 0.14
PSZ2G099.48+55.60	0.135 ± 0.015	0.096 ± 0.011	151 ± 17	3.31 ± 0.09
PSZ2G100.45-38.42	0.070 ± 0.007	0.048 ± 0.005	68 ± 7	2.682 ± 0.025
PSZ2G103.40-32.99	0.156 ± 0.029	0.107 ± 0.020	144 ± 27	2.45 ± 0.18
PSZ2G105.55+77.21	—	—	—	3.25 ± 0.09

Table 5.4: continued.

Name	A_{2D}	A_{3D}	$\sigma_{v,3D}$ km s $^{-1}$	kT keV
PSZ2G106.41+50.82	—	—	—	4.79 ± 0.12
PSZ2G107.10+65.32N	—	—	—	7.17 ± 0.27
PSZ2G107.10+65.32S	0.102 ± 0.013	0.070 ± 0.009	162 ± 21	7.17 ± 0.27
PSZ2G111.75+70.37	—	—	—	6.10 ± 0.23
PSZ2G113.29+29.69	—	—	—	4.53 ± 0.07
PSZ2G113.91+37.01	—	—	—	7.60 ± 0.25
PSZ2G114.79+33.71	—	—	—	4.66 ± 0.10
PSZ2G134.70+48.91	—	—	—	7.3 ± 0.8
PSZ2G136.92+59.46	0.105 ± 0.007	0.073 ± 0.005	114 ± 8	3.28 ± 0.17
PSZ2G137.74+27.08	—	—	—	2.94 ± 0.07
PSZ2G143.26+65.24	0.131 ± 0.016	0.089 ± 0.011	224 ± 28	8.50 ± 0.31
PSZ2G149.75+34.68	0.116 ± 0.009	0.080 ± 0.006	186 ± 15	7.24 ± 0.13
PSZ2G166.09+43.38	0.086 ± 0.008	0.061 ± 0.005	143 ± 13	7.35 ± 0.20
PSZ2G172.74+65.30	0.153 ± 0.012	0.110 ± 0.009	185 ± 15	3.80 ± 0.06
PSZ2G179.09+60.12	—	—	—	4.23 ± 0.07
PSZ2G182.59+55.83	—	—	—	6.30 ± 0.13
PSZ2G184.68+28.91	—	—	—	6.07 ± 0.19
PSZ2G186.37+37.26	0.068 ± 0.007	0.044 ± 0.005	114 ± 12	8.90 ± 0.20
PSZ2G187.53+21.92	—	—	—	6.25 ± 0.12
PSZ2G192.18+56.12	0.086 ± 0.008	0.062 ± 0.006	111 ± 10	4.29 ± 0.11
PSZ2G195.60+44.06W2	0.140 ± 0.011	0.089 ± 0.007	186 ± 15	5.91 ± 0.17

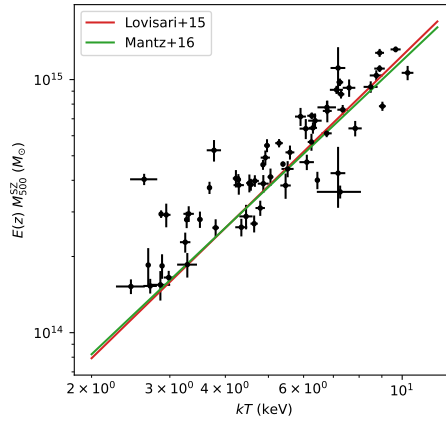


Figure 5.10: Mass versus temperature of our sample. The overplotted lines are scaling relations of Lovisari et al. (2015) (red) and Mantz et al. (2016) (green).

5.A Temperature measurements of the sample

We plotted mass versus temperature in Fig. 5.10. Though our spectral extraction region is $0.4r_{500}$, the measurements are close to the $M_{500} - kT_{500}$ scaling relation (e.g., Lovisari et al. 2015; Mantz et al. 2016).